Molecular Dynamics Simulations of the Melting of Aluminum Nanoparticles†

Saman Alavi*

Steacie Institute for Molecular Sciences, National Research Council of Canada, Ottawa, Ontario K1A 0R6, Canada

Donald L. Thompson*

Department of Chemistry, University of Missouri−Columbia, Columbia, Missouri 65211

Received: June 20, 2005; In Final Form: August 19, 2005

Molecular dynamics simulations are performed to determine the melting points of aluminum nanoparticles of 55−1000 atoms with the Streitz−Mintmire [*Phys. Rev. B* **1994**, *50*, 11996] variable-charge electrostatic plus potential. The melting of the nanoparticles is characterized by studying the temperature dependence of the potential energy and Lindemann index. Nanoparticles with less than 850 atoms show bistability between the solid and liquid phases over temperature ranges below the point of complete melting. The potential energy of a nanoparticle in the bistable region alternates between values corresponding to the solid and liquid phases. This bistability is characteristic of dynamic coexistence melting. At higher temperatures, only the liquid state is stable. Nanoparticles with more than 850 atoms undergo a sharp solid−liquid-phase transition characteristic of the bulk solid phase. The variation of the melting point with the effective nanoparticle radius is also determined.

1. Introduction

Here we present the results of a molecular dynamics (MD) study of the melting of aluminum nanoparticles. Bulk solid and liquid phases of materials are in equilibrium at a specific temperature and pressure, the melting point; however, the melting of nanoparticles is more complex. The nature of the melting process and the temperature at which a particle melts depends on its size. Of course, as the size of the particle increases the melting behavior and the melting point approach that of the bulk. Particles with radii ∼10 nm and larger can be treated with thermodynamic models,[1] although surface tension effects can cause the melting point to be lower than that of the bulk. The purpose of the present study is to develop a better understanding of the melting of various sizes of nanoparticles of aluminum, including magic number particles.

In small nanoparticles the liquid and solid phases can exist in dynamic equilibrium over a range of temperatures, much like the equilibrium between two chemical isomers. This behavior is called *dynamic coexistence melting*. For temperatures smaller than a specific value T_f the solid form is exclusively stable and for temperatures higher than T_m, the liquid form is exclusively stable, between T_f and T_m the nanoparticle fluctuates between the solid and liquid states, and the ratio of the solid and liquid states in an ensemble is given by $K = [\text{solid}]/[\text{liquid}] = \exp(\Delta G/kT)$, where ΔG is the free energy difference between the solid and liquid forms of the nanoparticle. Dynamic coexistence melting is now well understood in terms of the minima of the potential energy surfaces of nanoparticles[2−5] and is considered to be a first-order phase transition broadened by finite size effects.[6] Dynamic coexistence melting has been observed for rare-gas clusters with 19 or fewer atoms[2] and in a separate study of Lennard-Jones clusters with 55 and 147 particles.[6] Zhao et al.[7] have performed MD simulations of the melting of silver clusters with 13 to 3871 atoms interacting with an embedded-atom model (EAM) potential. They observed dynamic coexistence melting for nanoparticles of 13−116 atoms. The size range of dynamic coexistence is comparable to that for rare-gas nanoparticles. We observe dynamic coexistence melting over a large range of particle sizes in the present study.

Magic number effects are often observed in the dynamic coexistence melting range. Studies of the size dependence of melting points of Lennard-Jones[8,9] particles (up to 60 atoms) and sodium particles[10−13] (up to 200 atoms) show that the melting point varies nonmonotonically as the size of the particle decreases. Nanoparticles with a particular number of molecules can have melting points that are higher than those with only one or a few molecules more or less. These effects have been related to the completion of geometrical and electronic shells in magic number particles.[13] Some magic number effects are observed in the melting of aluminum nanoparticles studied in this work.

There can be significant differences in the charges on atoms in the interior and at the surface of metal or semiconductor materials. This can be particularly important in nanoparticles in which there are large variations in the atomic coordination and binding in different parts of a nanoparticle. As a result, fixed-charge potential energy functions cannot be used in molecular dynamics (MD) simulations of these materials. Ideally, one should use ab initio MD[14] to correctly treat the nonuniform electron distributions in nanoparticles of metals and semiconductors, but these calculations are presently confined to small systems of approximately 100 atoms. A practical alternative is a classical variable-charge potential model, such as the electrostatic plus (ES+) potential of Streitz and Mintmire.[15,16] This potential includes an electrostatic potential contribution and many-body embedded atom method (EAM) contribution and has been parametrized for aluminum and

† Part of the special issue "William Hase Festschrift".

* Corresponding authors. Saman Alavi: phone: (613)991-1237; fax: (613)947-2838; e-mail: saman.alavi@nrc.ca. Donald L. Thompson: phone: (573)882-0051; fax: (573)882-2754; e-mail: thompsondon@missouri.edu.

10.1021/jp053318s CCC: $33.50
Published on Web 09/23/2005

aluminum oxide. It has been applied to the calculation of surface and bulk properties; it accurately reproduces the lattice parameters, elastic constants, surface reconstructions, and cohesive eneregies.[15] The ES+ potential has been used in simulations of the reaction of a million-atom aluminum nanoparticle with gas-phase molecular oxygen.[17] These simulations predict a 40 Å thickness for the oxide coating formed on an aluminum surface exposed to gas-phase oxygen, in good agreement with experiment. It has also been used to study the oxidation of aluminum nanoparticles in the presence of limited amounts of oxygen.[18] In the present work we use the ES+ potential to study the physical properties of aluminum nanoparticles of up to 1000 atoms as functions of temperature. Our main focus is on characterizing the melting of the particles as a function of size.

The melting transitions of nanoparticles of different materials have been characterized by calculating various dynamic or structural properties at different temperatures. The properties used to characterize melting include the Lindemann index[19−21] (i.e., the root-mean-square bond length fluctuations),[2] static structure factors,[7] radial distribution functions, and many different types of energy-temperature or heat capacity-temperature plots.[2,7,20−24] In the present work we have used the potential energy and the Lindemann index to characterize melting in the aluminum nanoparticles. The potential energy of the nanoparticles gives a clear indication of structural change within the nanoparticles, and the Lindemann index shows that the change corresponds to a melting transition, not a transition to an amorphous solid structure.

2. The Potential

The electrostatic plus potential of Streitz and Mintmire[15] is used in the molecular dynamics calculations. This potential treats electrostatic charges on aluminum as simulation variables which are updated at every time step. The total potential energy U_{pot} is a function of the positions, $\{\mathbf{r}\}$, and charges, $\{q\}$, of the atoms and is composed of a long-range electrostatic contribution, U_{es}, and a short-range embedded-atom method (EAM) interaction U_{eam}:

$$U_{pot}(\{\mathbf{r},q\}) = U_{es}(\{\mathbf{r},q\}) + U_{eam}(\{\mathbf{r}\}) \quad (1)$$

The embedded atom contribution is the sum of a pair potential, ϕ_{ij}, and an attractive many-body embedding energy, F_i

$$U_{eam}(\{\mathbf{r}\}) = \sum_{i<j}\phi_{ij}(r_{ij}) - \sum_{i=1}^{N}F_i[P_i] \quad (2)$$

In the ES+ potential, the Finnis−Sinclair[25] functional dependence on the local electron density, P_i, from tight-binding theory is used to obtain the many-body contribution to the potential, $F_i[P_i] = -A_i\sqrt{P_i/\xi_i}$, where A_i and ξ_i are positive fitting constants. The local electron density of aluminum atom i is the sum of the electron densities from all the other atoms

$$P_i(r_i) = \sum_{i\neq j}\xi_j \exp[-\beta(r_{ij} - r^*)] \quad (3)$$

An exponential decay is chosen for the attractive part of the EAM potential. The residual pair interaction in eq 2 is

$$\phi_{ij}(r_{ij}) = 2B\exp\left[-\beta\left(\frac{r_{ij}-r^*}{2}\right)\right] - C[1+\alpha(r_{ij}-r^*)]\exp[-\alpha(r_{ij}-r^*)] \quad (4)$$

where β and α are related to the decay lengths of the repulsive and attractive parts of the residual pair potential, respectively, r^* is the equilibrium distance of the two-body potential, C is the two-body dissociation energy, and B is related to the number of nearest neighbors in the solid. The constants in these equations are taken as adjustable parameters. Further details of this potential are given in refs 15 and 25.

The electrostatic contribution to the potential has a single aluminum atom electrostatic energy component and a Coulombic pair-interaction component V_{ij}

$$U_{es}(\{\mathbf{r},q\}) = \sum_{i=1}^{N}(\chi^0 q_i + J^0 q_i^2) + \frac{1}{2}\sum_{i\neq j}V_{ij}(\mathbf{r_{ij}};q_i,q_j) \quad (5)$$

where χ^0 is the electronegativity and J^0 is the hardness of the aluminum atoms. The electronic charge density, ρ_i, is the sum of an effective nuclear charge, Z_i, and a valence-electron charge distribution, f_i:

$$\rho_i(\mathbf{r};q_i) = Z_i\delta(\mathbf{r}-\mathbf{r_i}) + (q_i - Z_i)f_i(|\mathbf{r}-\mathbf{r_i}|) \quad (6)$$

The ES+ potential assumes a spherical charge distribution for the valence electron cloud, $f_i(r_i) = (\zeta^3/\pi)\exp(-2\zeta r_i)$, where ζ is the decay length of the aluminum valence orbital. The Coulombic pair-interactions are obtained from charge densities about each aluminum atom, $V_{ij}(r_{ij};q_i,q_j) = \int\int d\mathbf{r_1}d\mathbf{r_2}\{\rho_i(\mathbf{r_1};q_i)\rho_j(\mathbf{r_2};q_j)\}/\{r_{12}\}$. The variable atomic charges, $\{q\}$, are determined by minimizing the electrostatic energy subject to the constraint of zero net charge, i.e., $\sum_{i=1}^{N}q_i = 0$. The values of the potential parameters are given in refs 15 and 18.

3. Simulation Methods

Molecular dynamics simulations of nanoparticles were performed for the NVT ensemble. The equations of motion were integrated using the leapfrog algorithm[26,27] with a time step of 2 fs. The long-range electrostatic forces between the atoms were calculated directly. During the simulations, the temperature was scaled every 10 time steps by velocity scaling. The nanoparticle structures were annealed for 40 ps, and then data were gathered over 360 ps.

Variations in the potential energy and the Lindemann index as functions of temperature were used to identify the melting point. The Lindemann index has been extensively used to characterize the melting transition of nanoparticles.[28] In nonperiodic systems, the Lindemann index is more convenient to use than the diffusion coefficient since in the calculation of the relative separation of atoms, the center of mass motion and rotation of the nanoparticle do not have to be first eliminated from the motion of the individual atoms. The Lindemann index is the relative root-mean-square bond-length fluctuation, δ, defined as

$$\delta = \frac{2}{N(N-1)}\sum_{i<j}\frac{\sqrt{\langle r_{ij}^2\rangle_t - \langle r_{ij}\rangle_t^2}}{\langle r_{ij}\rangle_t} \quad (7)$$

where r_{ij} is the separation of atoms i and j, and $\langle\ \rangle_t$ indicates a time average. The atoms in a solid undergo small amplitude vibrations about equilibrium lattice sites and the Lindemann

index is small, with the root-mean-square (rms) deviations in the bond lengths being less than 2%. At the melting point, the molecules gain some translational freedom, and this index can increase by as much as a factor of 3.

4. Results and Discussion

It is useful to investigate how the predictions of the Streitz−Mintmire ES+ potential compare with predictions of the commonly used Sutton−Chen[29] potential, which was developed to describe various metals. We compare the structures obtained by simulated annealing MD with the Steitz-Mintmire ES+ potential for aluminum nanoparticles with the structures that have been reported for other metal nanoparticles using the Sutton−Chen EAM potential. Note that we did not attempt to determine the global minima for the particles. Simulated annealing is not an appropriate method for determining the global minimum-energy structure for particles bigger than 100 atoms; however, a structure close to the minimum energy structure can be obtained. The energy landscape near the minimum is expected to be relatively flat for a large nanoparticle, and for the range of temperatures of interest, numerous local potential minima will be accessible. However, for the small nanoparticles for which we make comparisons with the Sutton−Chen potential, we can be confident that our simulated annealing method has determined the global mimima.

The minimum energy structures of metal nanoparticles interacting with the Sutton−Chen[29] EAM potential were determined by a Monte Carlo minimization method by Doye and Wales.[30,31] The Sutton−Chen potential has the form

$$E = \epsilon \sum_i \left[\frac{1}{2} \sum_{j \neq i} \left(\frac{a}{r_{ij}} \right)^n - c\sqrt{\rho_i} \right] \tag{8}$$

where the local atomic density, ρ_i, is given by

$$\rho_i = \sum_{j \neq i} \left(\frac{a}{r_{ij}} \right)^m \tag{9}$$

The parameters n and m are positive exponents with $n > m$, where n characterizes the repulsive part of the potential and m characterizes the attractive part. Aluminum is described by a $(n,m) = (7,6)$ potential, whereas a (12,6) potential is used of Ag and Rh, a (9,6) potential for Ni and Cu, and a (10,8) potential for Au and Pt. Doye and Wales[30,31] determined the minimum energy structures for the (12,6), (9,6), and (10,8) cases for nanoparticles with up to 80 atoms. Joswig and Springborg[32] recently determined global minimum energy structures for (7,6) aluminum nanoparticles with up to 60 atoms using a genetic algorithm search routine. For many nanoparticle sizes, the global minimum energy structures of metallic nanoparticles are different from the Lennard-Jones analogues.[31,33−40] The Lennard-Jones magic number particles (13, 55, 147, ... atoms) have icosahedral structures, and particles of other sizes have icosahedra cores with incomplete shells. The metallic nanoparticles do not necessarily form icosahedral-based structures. Several examples of nonicosahedral metallic nanoparticles are discussed in the paragraph below.

Structures of the aluminum nanoparticles with 13−20 atoms determined by simulated annealing MD with the ES+ potential at 200 K are shown in Figure 1. A number of the nanoparticles (with 13, 14, 15, 17, 19, and 20 atoms) are similar to those determined from the Sutton−Chen (9,6) potential.[30] The interesting exception is the 16-atom nanoparticle which has a structure similar to that determined for the Sutton−Chen (7,6) potential.[32] The structures of the 13- and 15-atom nanoparticles are similar in the (9,6) and (7,6) potentials. Nanoparticles with 55, 147, 309, 561, and 923 atoms correspond to closed shell ideal icosahedral structures for Lennard-Jones nanoparticles. Deviations from the ideal icosahedral structures are seen for the 55-atom nanoparticle with the Sutton−Chen potential.[32] The Streitz−Mintmire potential for these nanoparticles also show deviations from the ideal structures.

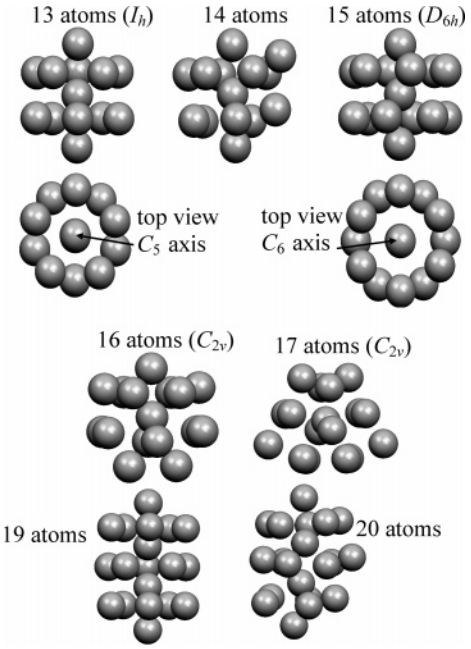

Figure 1. Structures and point groups of aluminum nanoparticles with 13, 14, 15, 16, 17, 19, and 20 atoms. The 13-, 14-, 19-, and 20-atom nanoparticles correspond to the structures observed for the LJ and Sutton−Chen potentials.

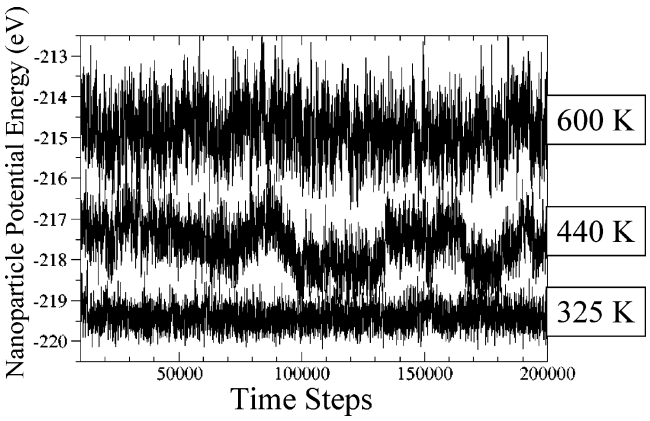

Figure 2. The potential energy (in eV units) as a function of simulation time computed by using eq 1 for the aluminum nanoparticle with 75 atoms for 325, 440, and 600 K during the equilibrium segments of the simulations. The 440 K isotherm shows bistability between a low-energy solid phase and a high-energy liquid phase. The probability of residing in each state is proportional to the time spent in that state.

The average potential energy per atom in a nanoparticle of N atoms is determined during the equilibrium stage of each simulation. Sample trajectories at 325, 440, and 600 K for the 75-atom nanoparticle are shown in Figure 2. The total potential energy of the 325 and 600 K trajectories converge to a single value; however, the potential energy of trajectory at 440 K jumps between low values, corresponding to the solid state of the nanoparticle, and high values, which correspond to the liquid state; that is, the particle undergoes *dynamic coexistence melting*. In the bistable regime, the probability of the nanoparticle being

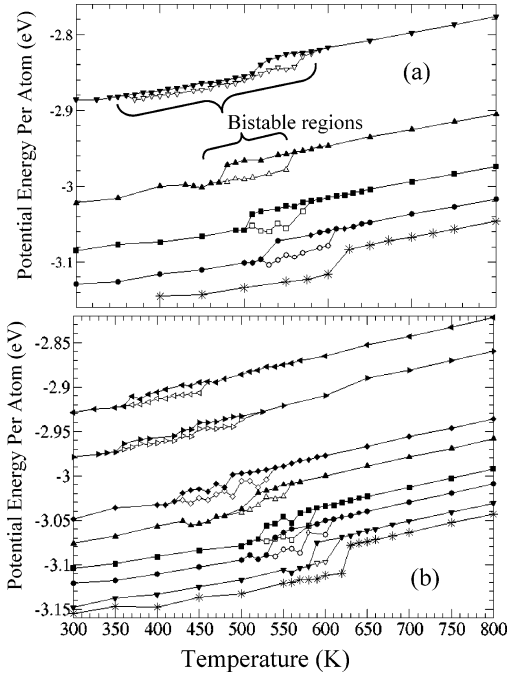

Figure 3. (a) The variation of the potential energy per atom (in eV) as a function of the temperature for the magic number aluminum nanoparticles with 55 (▼), 147 (▲), 309 (■), 561(●), and 923 (*) atoms. The bistable region shifts to higher temperatures as the size of the nanoparticle increases and disappears all together for the 923 nanoparticle. (b) The variation of the potential energy per atom as a function of the temperature for aluminum nanoparticles with 75 (solid triangle turned to the left), 108 (solid triangle turned to the right), 200 (◆), 256 (▲), 395 (■), 500 (●), 700 (▼), and 865 (*) atoms. The bistable region shifts to higher temperatures as the size of the nanoparticle increases and disappears for the 865 nanoparticle.

solid can be determined by calculating the fraction of time in which the nanoparticle is in the low potential energy part of the trajectory. As the temperature of the trajectories is increased, the probability of the nanoparticle residing in the solid state decreases, and finally a temperature is reached at which the nanoparticle only is stable in the liquid state.

The potential energy per aluminum atom as a function of temperatures for nanoparticles with different numbers of atoms is shown in Figure 3. Plots of the potential energy per atom for the magic number nanoparticles with 55, 147, 309, 561, and 923 atoms are shown in Figure 3(a) and those for 75, 108, 200, 256, 395, 500, 700, and 865 in Figure 3(b). In the bistable temperature range, both solid and liquid limits of the potential energy are shown. It is seen in this figure that the range of bistability shifts to higher temperatures as the size of the nanoparticle increases. Also the bistable range becomes shorter for larger nanoparticles. For large nanoparticles (from 923 atoms in Figure 3(a)), bistability is no longer observed, and the melting behavior becomes similar to bulk melting. Figure 3(b) shows the same plots for other nanoparticles ranging from 75 to 864 atoms.

The high values of the potential energy per atom in both solid and liquid states for the small nanoparticles are a reflection of the high fraction of undercoordinated surface atoms. In larger nanoparticles, the proportion of interior atoms increases, and the average potential energy per atom converges to the bulk value. This is seen in Figure 3, where the values of the average potential energy of the larger nanoparticles approach limiting values and are much closer to each other than those of the smaller nanoparticles. The average potential energy per atom in the nanoparticle is equivalent to the cohesive energy per atom.

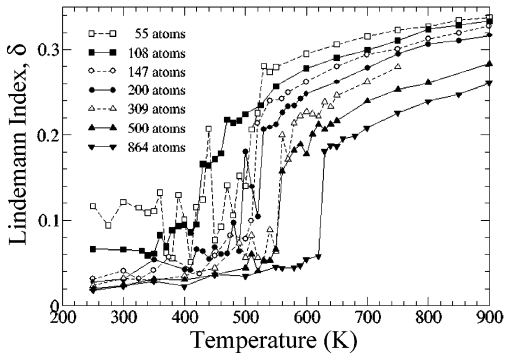

Figure 4. The variation of the Lindemann index, eq 9, with temperature for selected nanoparticle sizes. The magic number nanoparticles data are shown with empty symbols and dashed lines. The 55- and 147-atom nanoparticles melt at temperatures higher than do their close neighbors.

For the large nanoparticles at 300 K, the average potential energy per atom approaches the limit of ≈3.15 eV/atom. This is consistent with the experimental[41] and theoretical[15] (predicted by the Steitz-Mintmire ES+ potential) cohesive energy of 3.39 eV/atom for bulk fcc aluminum.

The potential energy plots shown in Figure 3 are a strong indication of the melting of the nanoparticles. However, similar behavior could result from a solid−solid or solid−glass phase transition. To unambiguously establish that a solid to liquid transition has occurred, the Lindemann index, which shows the dynamic behavior of the atoms in the nanoparticles, is calculated. The calculated temperature variation of the Lindemann index for aluminum nanoparticles is shown in Figure 4. At low temperatures the value of the Lindemann index is small (generally less than 0.05). With the onset of dynamic coexistence between the solid and liquid phases, the value of the Lindemann index increases due to contributions from the liquid phase and finally stabilizes at values about three times the original low-temperature value.

For the 108-atom nanoparticle, shown by solid squares in Figure 4, the value of the Lindemann index is initially stable at a value near 0.06. As the temperature reaches ≈ 350 K, the Lindemann index begins to increase, with fluctuations appearing at several temperatures. After 500 K, the value of the Lindemann index increases monotonically. The beginning of the increase in the Lindemann index at about 350 K corresponds with the beginning of the bistable region in the potential energy curve of Figure 3(b) (see the temperature regions with both filled and unfilled symbols). The higher temperature region where the Lindemann index varies monotonically (T > 500 K) is in the liquid range of the 108-atom nanoparticles. This liquid region of the Lindemann index curve may also be compared with the similar temperature range of the potential energy curves in Figure 3.

The other nanoparticle sizes show similar behavior. The Lindemann index is initially stable at a low value, up to a certain temperature, above which it starts to increase and fluctuate. This shows the onset of bistability. After a sharp rise, the Lindemann index will then increase monotonically as temperature is increased. For solid nanoparticles with more than approximately 100 atoms, at low temperatures the atoms are confined to fixed sites, and the Lindemann index converges to a value between 0.02 and 0.03 which is characteristic of bulk phases. After melting, the Lindemann index of the liquid nanoparticles depends on the size of the nanoparticle. For large nanoparticles a greater percentage of the atoms is confined to the core and have less translational freedom. This leads to the decrease in

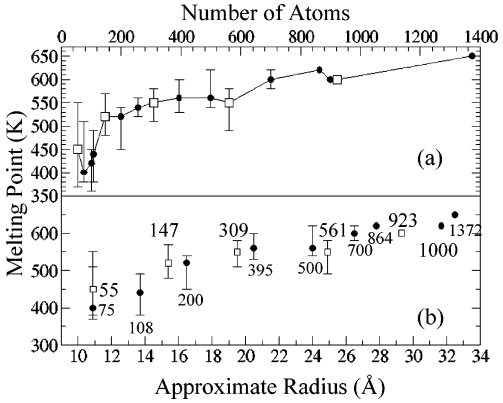

Figure 5. (a) The variation of the melting point as a function of the number of atoms in the nanoparticle. The results for the 55-, 147-, 309-, 561-, and 923-atom nanoparticles are shown with empty symbols, and the other nanoparticles are shown with full symbols. The melting points are taken to be the temperature at which there is a sharp rise in the Lindemann index; the "error bars" are the lower and upper bounds of the bistable region determined from the potential energy studies. Magic number effects are seen for the 55- and 147-atom nanoparticles; the melting points of larger nanoparticle generally increase monotonically with size. (b) The variation of the melting point with the effective radii of the nanoparticles. The number of atoms in each nanoparticle is given for each point. Magic number nanoparticles are shown with the white square symbols.

the Lindemann index for the larger nanoparticles seen at high temperatures in Figure 4.

The melting points (determined from the temperature where the Lindemann index shows a sharp increase) and melting temperature range (from the potential energy plots) are shown in Figure 5(a) as functions of the nanoparticle size. The magic number nanoparticles are shown with the empty symbols and the other nanoparticles with the filled symbols. The melting point is chosen based on the Lindemann index, and the "error bars" determine the range of bistability for each nanoparticles. The lower temperature limit for each point is the onset of bistability, and the upper limit is the temperature at which only the liquid state is stable. For nanoparticles with up to about 200 atoms, the melting point does not vary monotonically and shows some magic number effects. The bistable temperature range becomes smaller as the size of the nanoparticle increases.

The size dependence of the melting point for large nanoparticles of metals has been studied experimentally[1a,24,42,43] and theoretically.[7,44,45] A classical thermodynamic model for the melting point T_m of a nanoparticle as a function of the radius r was given by Hanszen[45]

$$T_0 - T_m = \frac{2T_0}{\Delta H_0}\left[\frac{\sigma_{sl}}{\rho_s(r - t_0)} + \frac{\sigma_{lv}}{r}\left(\frac{1}{\rho_s} - \frac{1}{\rho_l}\right)\right] \qquad (10)$$

where T_0 is the bulk melting temperature, ΔH_0 is the bulk enthalpy of melting, σ_{sl} and σ_{lv} are the solid−liquid and liquid−vapor surface tensions, respectively, and ρ_s and ρ_l are the densities of the bulk solid and liquid phases, respectively. The parameter t_0 is defined as the critical thickness of the liquid layer on the nanoparticle at T_m and is usually taken as an adjustable parameter. This relation predicts $1/r \propto 1/N^{1/3}$ dependence of the nanoparticle melting point with size. The thermodynamic assumptions of eq 10 are valid only for "large" nanoparticles. The melting mechanism for large nanoparticles is called surface premelting.[1b] The predictions of eq 10 have been used to compare the calculated radius dependence of the melting point of tin nanoparticles larger than 50 Å with experimental measurements.[1a,24] Shi[44] has used a different thermodynamic model and experimental results to describe the melting of large nanoparticles with radii larger than approximately 20 Å. Our results for Al are consistent with these sizes for the surface premelting mechanism. Our calculations show that nanoparticles of Al larger than ≈25 Å (≈800 atoms) exhibit surface premelting behavior. The theoretical calculations of Zhao et al.[7] using eq 10 have been extended to nanoparticles of silver with radii as low as 12 Å which contain approximately 260 atoms. Kusche et al.[48] observed that the melting point of free sodium clusters change in an irregular manner with large fluctuations for nanoparticles of up to 200 atoms, which are smaller than that required to the thermodynamic surface premelting regime.

The shapes of the aluminum nanoparticles computed in the present study are generally nonspherical, thus an effective radius was assigned based on sampling the diameter of the nanoparticle in various directions. In Figure 5(b), the melting point is plotted as a function of the effective radii of the nanoparticles. Because of the size ranges for which the surface premelting mechanism is valid (as discussed in the previous paragraph), only the melting points of the large nanoparticle which do not show bistability (i.e., 800 atoms or more) can be described by eq 10. The melting points of the smaller nanoparticles deviate from eq 10. The experimental melting point of bulk aluminum metal is 933.5 K.[46] The largest nanoparticle in the simulations with 1000 atoms has still not reached the bulk limit in terms of its melting behavior. Very large sizes (on the order of 10^4 atoms) are required for metal nanoparticles to reach the bulk melting point.[47,48]

5. Summary and Conclusions

Molecular dynamics simulations of aluminum nanoparticles were carried out using the Streitz−Mintmire ES+ potential. The structures of some of the smaller nanoparticles are consistent with those determined with the Sutton−Chen EAM potential;[29−31] however, the structures determined from the ES+ potential do not agree with those for a single set of (n,m) values in eqs 7 and 8. The melting of selected aluminum nanoparticles with up to 1000 atoms has been characterized by calculating the potential energy per atom and the Lindemann index. Nanoparticles with fewer than 850 atoms show dynamic coexistence melting where solid and liquid phases are stable over a range of temperatures. The temperature range of bistability becomes narrower and shifts to higher temperatures as the size of the nanoparticle increases. For the smaller nanoparticles, magic number effects are pronounced, and nanoparticles with complete icosahedral shells have melting points higher than some of their neighboring nanoparticles. As the size of the nanoparticles increases, the variation of the melting point becomes more monotonic.

Acknowledgment. D.L.T. gratefully acknowledges support by the U.S. Army Research Office under grant number DAAD19-01-1-0503. S.A. gratefully acknowledges the support of the National Research Council of Canada.

References and Notes

(1) (a) Lai, L.; Guo, J. Y.; Petrova, V.; Ramanath, G.; Allen, L. H. *Phys. Rev. Lett.* **1996**, *77*, 99. (b) Wronski, C. R. M. B. *J. Appl. Phys.* **1967**, *18*, 1731. (c) Skripov, V. P.; Koverda, V. A.; Skokov, V. N. *Phys. Status Solidi A* **1981**, *66*, 109.

(2) Beck, T. L.; Jellinek, J.; Berry, R. S. *J. Chem. Phys.* **1987**, *87*, 545.

(3) Kunz, R.; Berry, R. S. *Phys. Rev. E* **1994**, *49*, 1895.

(4) Wales, D. J.; Berry, R. S. *Phys. Rev. Lett.* **1994**, *73*, 2875.
(5) Ball, K. D.; Berry, R. S.; Kunz, R. E.; Li, F.-Y.; Proykova, A.; Wales, D. J. *Science* **1996**, *271*, 963.
(6) Labastie,P.; Whetten, R. L. *Phys. Rev. Lett.* **1990**, *65*, 1567.
(7) Zhao, S. J.; Wang, S. Q.; Cheng, D. Y.; Ye, H. Q. *J. Phys. Chem. B* **2001**, *105*, 12857.
(8) Wales,D. J.; Berry, R. S. *J. Chem. Phys.* **1990**, *92*, 4283.
(9) Frantz, D. D. *J. Chem. Phys.* **2001**, *115*, 6136.
(10) Kusche, P.; Hippler, T.; Schmidt, M.; von Issendorff, B.; Haberland, H. *Eur. Phys. J. D* **1999**, *9*, 1.
(11) Schmidt, M.; Hippler, Th.; Donges, J.; Kronmüller, W.; von Issendorff, B.; Haberland, H.; Labastie, P. *Phys. Rev. Lett.* **2001**, *87*, 203402.
(12) Schmidt, M.; Donges, J.; Hippler, Th.; Haberland, H. *Phys. Rev. Lett.* **2003**, *90*, 103401.
(13) Calvo, F.; Spiegelmann, F. *J. Chem. Phys.* **2000**, *112*, 2888.
(14) Car, R.; Parrinello, M. *Phys. Rev. Lett.* **1983**, *55*, 2471.
(15) Streitz, F. H.; Mintmire, J. W. *Phys. Rev. B* **1994**, *50*, 11996.
(16) Keffer, D. J.; Mintmire, J. W. *Int. J. Quantum Chem.* **2000**, *80*, 733.
(17) Campbell, T.; Kalia, R. J.; Nakano, A.; Vashishta, P.; Ogata, S.; Rodgers, S. *Phys. Rev. Lett.* **1999**, *82*, 4866.
(18) Alavi, S.; Mintmire, J. A.; Thompson, D. L. *J. Phys. Chem. B* **2005**, *109*, 209.
(19) Lindemann, F. A. *Phys. Z.* **1910**, *11*, 609.
(20) Proykova, A.; Pisov, S.; Radev, R.; Mihailov, P.; Daykov, I.; Berry, R. S. *Vacuum* **2003**, *68*, 87.
(21) (a) Kristensen, W. D.; Jensen, E. J.; Cotterill, R. M. J. *J. Chem. Phys.* **1974**, *60*, 4161. (b) Briant, C. L.; Burton, J. J. *J. Chem. Phys.* **1975**, *63*, 2045. (c) Etters, R. D.; Kaelberer, J. B. *Phys. Rev. A* **1975**, *11*, 1068. (d) Kaelberer, J. B.; Etters, R. D. *J. Chem. Phys.* **1977**, *66*, 3233. (d) Etters, R. D.; Kaelberer, J. B. *J. Chem. Phys.* **1977**, *66*, 5112.
(22) Del Mistro, G.; Stace, A. J. *J. Chem. Phys.* **1993**, *98*, 3905.
(23) Shah, P.; Roy, S.; Chakravarty, C. *J. Chem. Phys.* **2003**, *118*, 10671.
(24) Bachels, T.; Güntherodt, H. J.; Schäfer, R. *Phys. Rev. Lett.* **2000**, *85*, 1250.
(25) Finnis, W.; Sinclair, J. E. *Philos. Mag. A* **1983**, *50*, 1285.
(26) Allen, M. P.; Tildesley, D. J. *Computer Simulation of Liquids*; Oxford University Press: Oxford, 1987.
(27) Frenkel, D.; Smit, B. *Understanding Molecular Dynamics*, 2nd ed.; Academic Press: San Diego, 2002.
(28) (a) Berry, R. S.; Jellinek, J.; Natanson, G. *Phys. Rev. A* **1984**, *30*, 919. (b) Lee, Y. J.; Lee, E. K.; Kim, S.; Nieminen, R. M. *Phys. Rev. Lett.* **2001**, *86*, 999. (c) Zhou, Y.; Karplus, M.; Ball, K. D.; Berry, R. S. *J. Chem. Phys.* **2002**, *116*, 2323. (d) Westergren, J.; Nordholm, S.; Roœen, A. *Phys. Chem. Chem. Phys.* **2003**, *5*, 136.
(29) Sutton, A. P.; Chen, J. *Philos. Mag. Lett.* **1990**, *61*, 139.
(30) Doye, J. P. K.; Wales, D. J. *New J. Chem.* **1998**, *22*, 733.
(31) Cambridge Cluster Data Base: http://www-wales.ch.cam.ac.uk/CCD.html.
(32) Joswig, J.-O.; Springborg, M. *Phys. Rev. B* **2003**, *68*, 085408−1.
(33) Mackay, A. L. *Acta Crystallogr.* **1962**, *15*, 916.
(34) Farges, J.; de Feraudy, M. F.; Raoult, B.; Trochet, G. *Acta Crystallogr. A* **1982**, *38*, 656.
(35) Northby, J. A. *J. Chem. Phys.* **1987**, *87*, 6166.
(36) Wales, D.; Doye, J. P. K. *J. Phys. Chem. A* **1997**, *101*, 5111.
(37) Doye, J. P. K.; Wales, D. J.; Miller, M. A. *J. Chem. Phys.* **1998**, *109*, 8143.
(38) Romero, D.; Barrón, C.; Gómez, S. *Comput. Phys. Commun.* **1999**, *123*, 87.
(39) Xiang, Y.; Jiang, H.; Cai, W.; Shao, X. *J. Phys. Chem. A* **2004**, *108*, 3586.
(40) Xiang, Y.; Cheng, L.; Cai, W.; Shao, X. *J. Phys. Chem. A* **2004**, *108*, 9516.
(41) Kittel, C. *Introduction to Solid-State Physics*, 5th ed.; Wiley: New York, 1976.
(42) Buffet, P.; Borel, J. P. *Phys. Rev. A* **1976**, *13*, 2287.
(43) Goldstein, A. N.; Echer, C. M.; Alivisatos, A. P. *Science* **1992**, *256*, 1425.
(44) Shi, F. G. *J. Mater. Res.* **1994**, *9*, 1307.
(45) Hanszen, K.-J. *Z. Phys.* **1960**, *157*, 523.
(46) *CRC Handbook of Chemistry and Physics*, 76th ed.; CRC Press: Boca Raton, FL, 1995.
(47) Bachels, T.; Günterodt, H. J.; Schäfer, R. *Phys. Rev. Lett.* **2000**, *85*, 1250.
(48) Kusche, R.; Hippler, T.; Schmidt, M.; von Issendorf, B.; Haberland, H. *Eur. Phys. J.* **1999**, *9*, 1.